LAWRENCE
LIVERMORE
NATIONAL
LABORATORY

LLNL-JRNL-827313

Investigating Dry Room Compatibility of Sulfide Solid-State Electrolytes for Scalable Manufacturing

Y. T. Chen, M. A.T. Marple, D. H. S. Tan, S. Y. Ham, B. Sayahpour, W. K. Li, H. Yang, E. A. Wu, J. M. Doux, J. Jang, P. Ridley, A. Cronk, G. Deysher, Z. Chen, Y. S. Meng

September 30, 2021

Journal of Materials Chemistry A

Disclaimer

Investigating Dry Room Compatibility of Sulfide Solid-State Electrolytes for Scalable Manufacturing

Yu-Ting Chen[1], Maxwell A. T. Marple[2], Darren H. S. Tan[3], So-Yeon Ham[1], Baharak Sayahpour[1], Wei-Kang Li[3], Hedi Yang[3], Jeong Beom Lee[4], Hoe Jin Hah[4], Erik A. Wu[3], Jean-Marie Doux[3], Jihyun Jang[3], Phillip Ridley[3], Ashley Cronk[1], Grayson Deysher[1], Zheng Chen[1,3,5,6]*, and Ying Shirley Meng[1,3,5]*

[1] Program of Materials Science and Engineering, University of California San Diego, La Jolla, California 92093, United States

[2] Physical and Life Science Directorate, Lawrence Livermore National Laboratory, Livermore, California 94550, United States

[3] Department of NanoEngineering, University of California San Diego, La Jolla, California 92093, United States of America

[4] LG Energy Solution, Ltd., LG Science Park, Magokjungang 10-ro, Gangseo-gu, Seoul 07796, Korea.

[5] Sustainable Power & Energy Center (SPEC), University of California San Diego, La Jolla, California 92093, United States

[6] Program of Chemical Engineering, University of California San Diego, La Jolla, California 92093, United States

* shmeng@ucsd.edu (Y. S. M.), zhengchen@eng.ucsd.edu (Z. C.)

Keywords: Solid-state electrolyte, Sulfide, LPSCl, Dry room, Stability

Abstract

All-solid-state batteries (ASSBs) are viewed as promising next-generation energy storage devices, due to their enhanced safety by replacing organic liquid electrolytes with non-flammable solid-state electrolytes (SSEs). The high ionic conductivity and low Young's modulus of sulfide SSEs make them suitable candidates for commercial ASSBs. Nevertheless, sulfide SSEs are generally reported to be unstable in ambient air. Moreover, instead of gloveboxes used for laboratory scale studies, large scale production of batteries is usually conducted in dry rooms. Thus, this study aims to elucidate the chemical evolution of a sulfide electrolyte, Li_6PS_5Cl (LPSCl), during air exposure and to evaluate its dry room compatibility. When LPSCl is exposed to ambient air, hydrolysis, hydration, and carbonate formation can occur. Moreover, hydrolysis can lead to irreversible sulfur loss and therefore LPSCl cannot be fully recovered in the subsequent heat treatment. During heat treatment, exposed LPSCl undergoes dehydration, decomposition of carbonate species, and reformation of the LPSCl phase. Finally, LPSCl was found to exhibit good stability in a dry room environment and was subject to only minor conductivity loss due to carbonate formation. The dry room exposed LPSCl sample was tested in a $LiNi_{0.8}Co_{0.1}Mn_{0.1}O_2$ | LiIn half-cell,

exhibiting no significant loss of electrochemical performance compared with the pristine LPSCl, proving it to be compatible with dry room manufacturing processes.

Table of Contents

When exposed to moisture, Li_6PS_5Cl undergoes both hydrolysis and hydration reactions. Li_6PS_5Cl can be partially recovered by heat treatment, but hydrolysis causes the formation of LiCl, Li_2S, Li_3PO_4, and oxysulfides due to the irreversible sulfur loss.

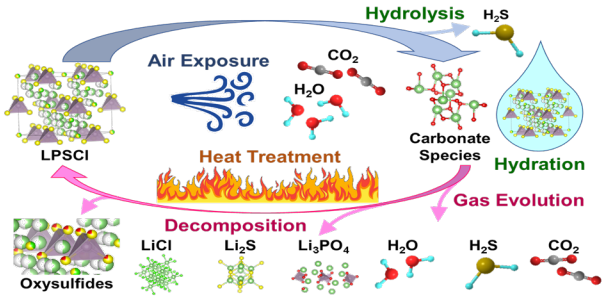

Introduction

All-solid-state batteries (ASSBs) are viewed as promising candidates for next-generation energy storage media.[1] Unlike conventional Li-ion batteries, ASSBs utilize non-flammable solid-state electrolytes (SSEs), which results in improved safety during operation.[2-5] Among SSEs, oxide-based and sulfide-based materials are the two types that draw the most attention.[6] Furthermore, sulfide electrolytes generally exhibit higher ionic conductivity, some of which are comparable to those of liquid electrolytes.[6-9] This property has been one of the main focuses in the literature, as high conductivity is necessary for enabling high power density batteries. Another advantage of sulfide SSEs is their lower Young's modulus, as softer electrolytes are subject to less stress formation and contact loss resulting from volume change during cell operation.[6] However, sulfide SSEs generally exhibit lower chemical stability than oxides, and their ionic conductivities decrease rapidly when exposed to ambient atmosphere.[6] As such, they are generally handled inside inert-gas-filled gloveboxes. Unfortunately, the essential processes of scalable manufacturing of state-of-the-art Li-ion batteries are conducted in dry rooms rather than gloveboxes, mainly for cost and space considerations. Unlike in Ar-filled gloveboxes, O_2, CO_2, and moisture are all present in a dry room atmosphere and are expected to react with sulfides. Therefore, it is important to understand the influence of air exposure of sulfide SSEs and provide solutions to mitigate any negative effects.

Several studies have proposed methods to increase the air stability of sulfide SSEs. For example, Li_2S-P_2S_5 can be partially substituted with P_2O_5 where the inclusion of oxygen significantly enhanced the air stability of the material.[10-12] Another approach is to apply hard and soft acid and base theory by replacing a hard acid, like P, with soft acids, such as Sn and Sb, to form stronger bonds with S, a soft base.[13, 14] Several Sn- or Sb-based sulfide electrolytes, such as Li_4SnS_4 and Li_3SbS_4, have been developed and exhibit superior air stability compared to other sulfide-based electrolytes. However, these approaches result in reduced ionic conductivity. To mitigate this issue, a solid solution system consisting of Li_4SnS_4 and Li_3SbS_4 was also studied and achieved an improved ionic conductivity of one order of magnitude compared to its individual components.[14] Another approach consists of incorporating a thin 50 nm oxygen substitution layer, which was applied to the surface of Li_6PS_5Cl (LPSCl) to form a core-shell structure, showing both improved air stability and better preservation of the ionic conductivity.[11]

Despite the efforts invested in improving the air stability of sulfide electrolytes, most studies only assess the stability by measuring the ionic conductivity and H_2S evolution. As such, these studies usually fail to investigate the degradation mechanism of sulfide SSEs during air exposure. Secondly, the effects on post-heat treatment SSEs are also not investigated. On the contrary, these types of fundamental insights on electrolyte stability were recently provided in a halide SSE study, where multiple characterization techniques were employed to compare the structural and compositional changes after ambient air exposure, and reported that heat treating the exposed electrolytes at 260 °C under vacuum could recover their pristine ionic conductivity.[15] In this work, the humidity of the dry room atmosphere was controlled to approximately 100 ppm, which is significantly lower than that of ambient air and is commonly used in today's lithium-ion battery fabrication.[16] Interestingly, we observed exhibiting no significant loss of electrochemical performance. This may be the key to prolonging the exposure time for sulfide SSEs without significantly impairing their ionic conductivities, and hence, provide a pathway

toward the scalable production of ASSBs.

This work seeks to study the degradation mechanism of LPSCl during exposure to air and investigate the chemical reactions occurring during the recovery process. **Figure 1** presents a schematic of the exposure and recovery processes. LPSCl was first exposed to air for 24 hours (denoted as "air-Exp"), and then heat treated at 550°C (denoted as "air-HT"), as it is the annealing temperature for LPSCl, to investigate the effect of heat treatment on ionic conductivity.[17-23] To study a more extreme case, LPSCl was dissolved in water and then vacuum dried at room temperature (denoted as "water-Exp"), followed by a heat treatment at 550°C (denoted as "water-HT"). The chemical composition of the four samples were then analyzed with multiple characterization techniques such as X-ray powder diffraction (XRD), solid-state nuclear magnetic resonance (ss-NMR) spectroscopy, and both Raman and Fourier-transform infrared spectroscopy (FTIR) spectroscopy.[24] After the heat treatment, the conductivity of both air-Exp and water-Exp samples can be recovered by approximately 3 orders of magnitude. To further understand the chemical reactions during heat treatment, thermal gravimetric analysis (TGA) and differential scanning calorimetry (DSC) were employed, and additional samples were heat-treated at lower temperatures based on the results from thermal characterization. We found that hydrolysis (resulting in H_2S evolution, and thus sulfur loss) and hydration reaction both occur from moisture exposure. Finally, LPSCl samples were exposed in a dry room environment and exhibited a relatively minor ionic conductivity drop. The electrochemical performance of the dry room exposed electrolyte in a $LiNi_{0.8}Co_{0.1}Mn_{0.1}O_2$ (NCM811) half-cell was also maintained, implying that LPSCl is indeed compatible with dry room environments.

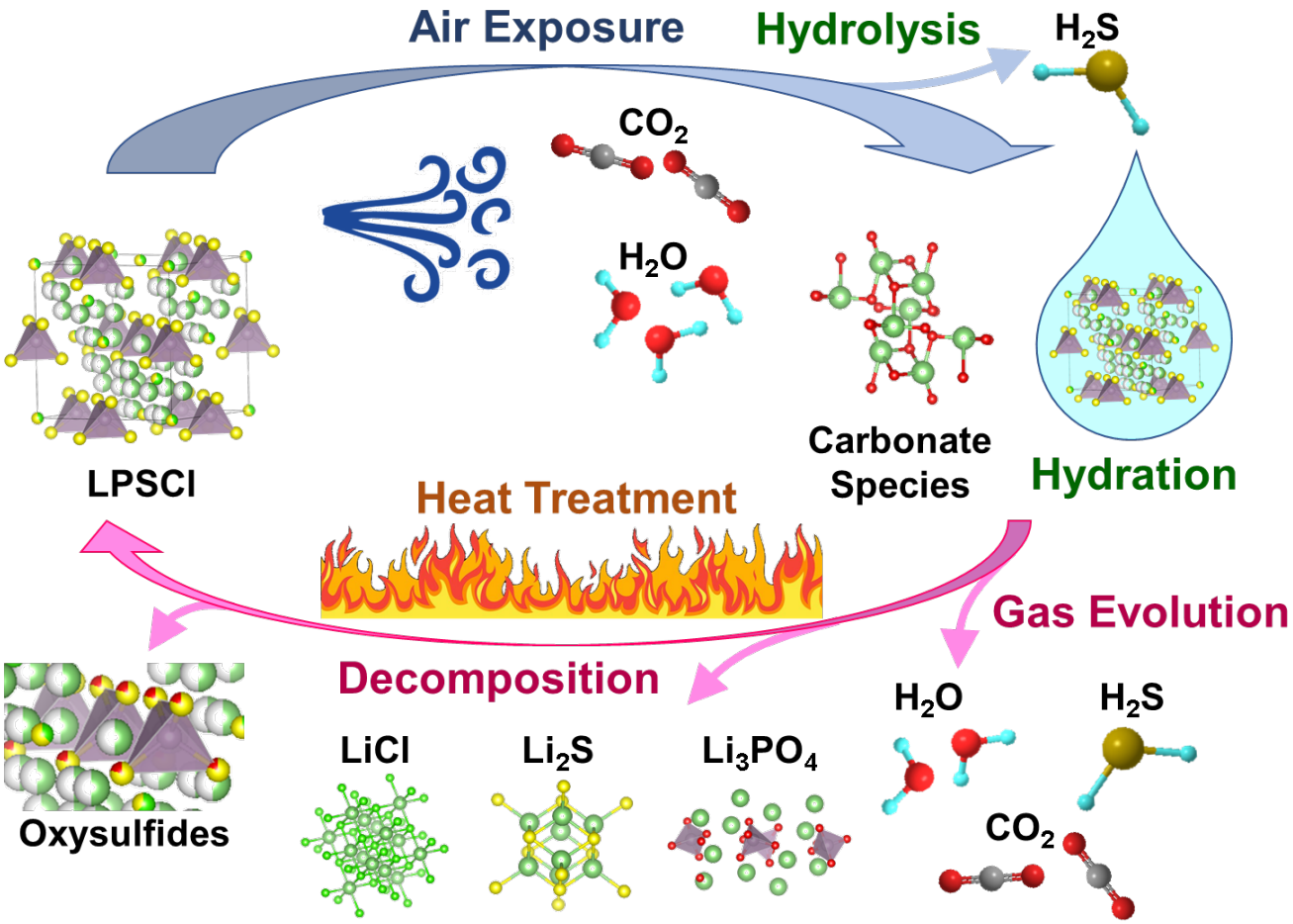

Figure 1. Schematic of the chemical reactions that occur when Li_6PS_5Cl is exposed to ambient air and during the subsequent heat treatment process.

Experimental

1. Exposure and heat treatment of LPSCl.

To prepare the air-exposed LPSCl sample (air-Exp), 300 mg of LPSCl (NEI) was evenly distributed in a 125 mL wide-mouth glass jar in an Ar-filled glovebox and then transferred to the antechamber with a total volume of 250 L. The chamber door was opened to expose the antechamber to ambient air (relative humidity between 45 to 55%) and closed after 1 minute of exposure. After 24 hours of exposure, the antechamber was vacuumed and purged with Ar, and the air-Exp sample was collected. The water-exposed LPSCl sample (water-Exp) was prepared by completely dissolving 1 g of LPSCl in 5 mL of water. The LPSCl aqueous solution was then vacuum dried at room temperature and the water-Exp sample was collected. 4 batches of 5 g LPSCl were evenly sprayed on petri dishes and placed in a dry room with a dew point of −45°C for 1, 2, 3 and 24 hours to obtain the dry room exposed samples. The exposed LPSCl samples were heat treated at designated temperatures under vacuum. In summary, 300 mg of LPSCl was placed inside a quartz tube with one end located in a muffle furnace. The other end was connected to a vacuum pump to remove all gases generated during the heat treatment process.

2. Electrochemical impedance spectroscopy (EIS), DC polarization, cyclic voltammetry (CV) and NCM811 half cells.

To avoid any air exposure, all the electrochemical tests were conducted in an Ar-filled glovebox. 70 mg of LPSCl sample was placed in a 10 mm PEEK die (**Figure S1**) and pressed at 370 MPa using titanium plungers to obtain a pellet with a thickness of about 0.55 mm (measured with a Vernier caliper). Vapor-grown carbon fibers (VGCF) were then added to both sides of the pellet and the cell was pressed again at 370 Mpa. After assembly, the cell was tightened in a cell holder. EIS measurements were performed from 1 MHz to 1 Hz, with an applied AC potential of 30 mV, using a Solartron 1260 Impedance Analyzer, at room temperature. The acquired Nyquist plots were analyzed with Z-View software. DC polarizations were obtained by applying a 1 V bias potential for 300 s using the Solartron SI 1287 Potentiostat.

To obtain the electrochemical windows for pristine, air-HT, and water-HT LPSCl samples, the powders were mixed with acetylene carbon at a weight ratio of 7:3 (LPSCl:C) using a Retsch Emax ball mill. LiIn alloy was prepared by mixing 30 mg of Li and 990 mg of In powder in a 20 mL sealed glass vial with a vortex mixer. LiIn alloy was used as both counter and reference electrode. Cyclic voltammetry was conducted using LPSCl-C | LPSCl | LiIn cells at a scan rate of 0.1 mV S^{-1} within 0 – 4.3 V voltage range vs Li. Three cycles were collected for each sample.

The $LiNi_{0.8}Co_{0.1}Mn_{0.1}O_2$ (NCM811, LG Chem) all-solid-state half-cell was constructed using 15 mg of NCM811 cathode composite, 70 mg of LPSCl samples, and 30 mg of LiIn alloy anode. NCM811 cathode composite was prepared by mixing NCM811, LPSCl samples, and vapor grown carbon fibers (Sigma-Aldrich) in a weight ratio of 66:31:3 in a mortar and pestle. The electrolyte and electrolyte powders were pressed at 370 MPa in the experimental setup described above and cycled using Neware Battery cyclers (A211-BTS-1U-ZWJ). Pristine LPSCl was used in the reference cell. Another cell was fabricated using dry room exposed (24 hours) LPSCl (including solid-state electrolyte separator layer and the cathode composite) to evaluate its electrochemical performance. All cells were cycled at C/10 in the 1st cycle and C/3 in the following cycles at 30°C (1 C = 200 mAh g^{-1}).[25]

3. Characterization.

X-ray diffraction (XRD) patterns of LPSCl samples were obtained by sealing the powders in 0.7 mm boron-rich glass capillaries in an Ar-filled glovebox. Measurements were taken using Cu Kα radiation (1.5406 Å) over a 2θ range of 10° to 65°, with a step size of 0.01°, using a Bruker/Nonius Microstar 592 diffractometer. Rietveld refinement was done using GSAS II software. Phase ratios and unit cells of Li_6PS_5Cl (ICSD 259200), Li_2S (ICSD 657596), LiCl (ICSD 26909) and Li_3PO_4 (ICSD 257440) were refined. Fourier transform infrared (FTIR) spectra with an attenuated total reflection (ATR) setup were measured with a Nicolet 6700 Fourier transform infrared spectrometer. Raman spectra were acquired with a Renishaw inVia upright microscope using 532 nm source. X-ray photoelectron spectroscopy was collected using The AXIS Supra XPS by Kratos Analytical. S 2*p*

and P 2*p* spectra were collected and analyzed with CasaXPS software. A spin-orbit coupling energy of 1.18 eV was used in S 2*p* fitting and 0.86 eV was used in P 2*p* fitting. The peak area ratio of 2*p* 1/2 and 2*p* 3/2 was fixed to 1:2. A NETZSCH STA 449 F3 Jupiter Simultaneous Thermal Analyzer with Coupled QMS 403 D Aëolos Mass Spectrometer were used to obtain TGA/DSC-MS data (monitoring 18, 34 and 44 molecular weight – corresponding to H_2O, H_2S and CO_2). 15-20 mg of LPSCl samples were placed in an Al_2O_3 pans (6.8 mm in diameter / 85 µL). The samples were prepared within 2 mins to minimize the air exposure. All measurements were conducted in Ar atmosphere, scanning from 30°C to 600°C at a scan rate of 10°C min^{-1}.

Solid-state ^{31}P and ^{7}Li magic angle spinning (MAS) NMR experiments were conducted on a 400 MHz Bruker Neo spectrometer operating at 161.97 and 155.5 MHz for ^{31}P and ^{7}Li, respectively. All samples were handled within an Ar glovebox and subsequently loaded into 4mm pencil-type ZrO_2 rotors with o-ring caps to prevent contamination with ambient air and moisture during the NMR experiments. The samples were spun at 10 kHz and the ^{31}P experiments were collected using a 2.68 µs π/2 pulse (RF field strength ~93 kHz), a recycle delay of 15 s for pristine and dry room LPSCl and 600 s for exposed and heat-treated samples, and with high power proton decoupling using spinal64. $\{^{1}H\}$-^{31}P cross polarization measurement were collected while spinning at 5 and 1.5 kHz, using a ^{1}H π/2 pulse of 2.25 µs (RF field strength ~111 kHz) and contact times of 1 ms or variable contact times from 0.25 ms to 5 ms for generating the CP build-up curves. Hydroxyapatite was used as a standard for setting up the $\{^{1}H\}$-^{31}P cross polarization measurements. ^{31}P spin lattice relaxation was measured with a saturation recovery experiment. 2D ^{1}H-^{31}P HETCOR was acquired while spinning at 5 kHz, using a short contact time (50 µs) and with a 60 s recycle delay. 2D acquisition was acquired using 128 hypercomplex points in t_1 with a 34 µs increment. The indirect ^{1}H dimension was referenced to tetramethylsilane (TMS) by setting the hydroxyl resonance of hydroxylapatite to δ_H = 0.2 ppm.[26] The ^{31}P chemical shift was externally referenced with respect to 85% H_3PO_4 by using the isotropic chemical shift of hydroxylapatite (δ_{iso}= 2.65 ppm). ^{7}Li spectra were collected while spinning at 10 kHz using a hard pulse (10° tip angle of 0.36 µs, RF field strength ~ 77 kHz) to obtain semi-quantitative spectra and with a recycle delay of 2 s. ^{7}Li spin lattice relaxation was measured using an inversion recovery pulse sequence with a π/2 and π pulse length of 2.68 and 5.36 µs, respectively. The ^{7}Li chemical shifts were externally referenced to the isotropic chemical shift of 1M LiCl (aq) (δ_{iso}=0 ppm). Deconvolution of the ^{31}P spectra was carried out using the software dmfit.[27]

Results and Discussion

To evaluate the influence of air and moisture exposure over the ionic conductivity of LPSCl, electrochemical impedance spectroscopy (EIS) was conducted. The results are summarized in **Figure 2a** and the Nyquist plots are presented in **Figure S2**. The ionic conductivity of the air exposed sample dropped from 2.92×10^{-3} to 9.50×10^{-7} S cm^{-1}, suggesting that exposure to ambient air largely degrades LPSCl. When LPSCl is dissolved in water, the ionic conductivity dropped even further to 4.67×10^{-8} S cm^{-1}. Nevertheless, a heat treatment at 550°C was able to partially recover the ionic conductivity of both samples by approximately 3 orders of magnitude. DC polarization was conducted on all the samples and confirmed that the electronic conductivity did not increase

following exposure and subsequent heat treatment (**Figure S3**). To investigate the origin of conductivity loss, XRD was conducted to probe the samples' phase compositions. After the exposure, the XRD patterns of both the air-Exp and water-Exp samples changed completely (**Figure S4**). LiCl can be observed in water-Exp sample, indicating decomposition of LPSCl when exposed to moisture. After the 550°C heat treatment, all the diffraction peaks in air-HT and water-HT samples can be attributed to four phases: LPSCl, LiCl, Li_2S, and Li_3PO_4.[28-31] Therefore, the diffraction patterns were refined and the results are shown in **Figure 2b**, **2c** and **Table S2**. Interestingly, the molar phase ratios of LiCl, Li_2S, and Li_3PO_4 in both samples are close to 1:1:1. Consequently, the net reaction after exposure and heat treatment can be described by the hydrolysis of LPSCl (equation 1):

$$Li_6PS_5Cl + 4\ H_2O \rightarrow LiCl + Li_2S + Li_3PO_4 + 4\ H_2S\uparrow \quad (1)$$

The hydrolysis of LPSCl will generate H_2S gas, resulting in permanent sulfur loss. Thus, LPSCl cannot be fully recovered after heat-treatment. The main difference between the air-HT and the water-HT samples is the amount of remaining LPSCl. Exposing LPSCl to a large excess of water will lead to more severe sulfur loss, and thus lower the LPSCl phase ratio after heat-treatment. As heat treated samples undergo partial decomposition, cyclic voltammetry (CV) was conducted to confirm whether the electrochemical windows changed (**Figure S5**). Both air-HT and water-HT exhibit similar oxidation (2.6 and 3.0 V) and reduction peaks (1.8 and 1.0 V) as pristine LPSCl. Nevertheless, the peak height decreases and can be related with the phase ratio of recovered LPSCl in each sample. Air-HT and water-HT samples also show new reduction (0.8 – 0 V) and oxidation (1.2 V) peaks. These may be attributed to decomposition products, as the peak height is again positively correlated to their phase ratios.

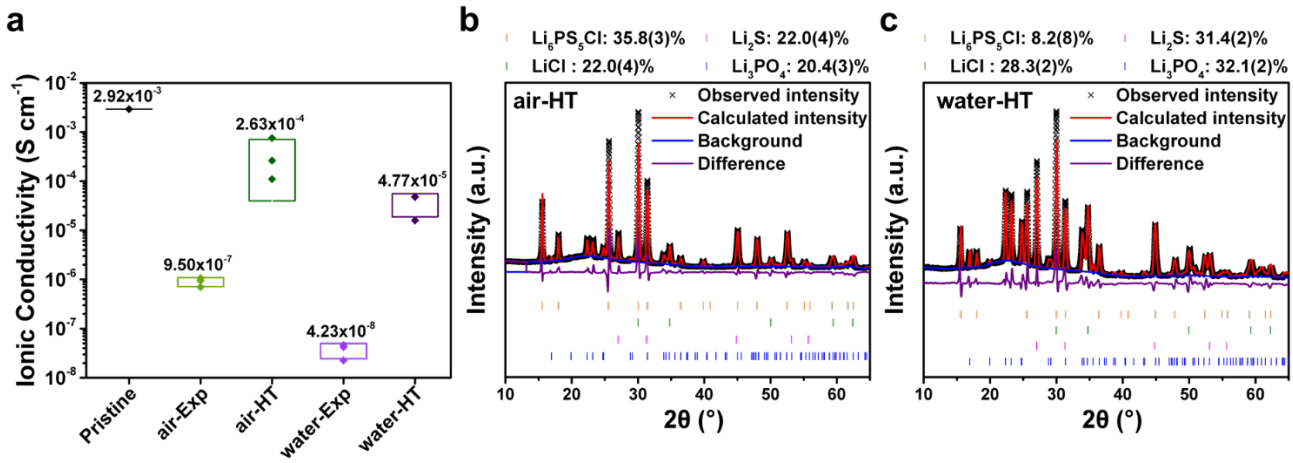

Figure 2. a) Ionic conductivity of the pristine, air, and water exposed LPSCl samples before and after heat treatment. All exposure and heat treatment conditions were conducted with three samples and median values are reported. Rietveld refinement results of the XRD patterns of b) the air exposed and heat-treated sample (air-HT) and c) the water exposed and heat-treated sample (water-HT). The molar phase ratios of all phases are labeled on top of the diffraction patterns.

As XRD reflects only the bulk properties of crystalline materials, more characterization methods were

subsequently conducted to probe the local chemical environment and nature of chemical bonding. **Figure S6** presents the S 2*p* and P 2*p* region spectra obtained by X-ray photoelectron spectroscopy (XPS). Pristine LPSCl exhibits an S 2*p* signal at 161.7 eV and a P 2*p* signal at 132.0 eV.[23] Li_2S signal at 160.3 eV was observed in both the air and water exposed samples, confirming that LPSCl decomposes in the presence of moisture. The water-Exp sample also exhibits a minor signal at 163.5 eV, which can be attributed to elemental sulfur or bridging sulfur atoms of Li_2S_n, resulting from the oxidation of S^{2-} during the exposure to water.[23, 32, 33] After the 550°C heat treatment, the amount of Li_2S increases and the SO_3^{2-} signal at 167.1 eV appears in both the air-HT and water-HT samples. Looking at the P 2*p* spectra, oxysulfides (PO_xS_y) at 133.0 eV form after exposure, and the intensity also increases after the heat treatment in both cases.[11] The P-O signal can be observed at 133.6 eV and 133.8 eV in the air-HT and water-HT samples, indicating the formation of Li_3PO_4.[34] The larger PS_4^{3-} peak area in air-HT than that of water-HT implies a larger degree of LPSCl recovery in air-HT sample. These are consistent with the previous XRD results.

The chemical bonds of exposed LPSCl were studied by both FTIR and Raman spectroscopy. The FTIR spectra (**Figure 3a**) show that both the air and water exposed samples exhibit evidence of hydration with a strong O-H stretching peak at 3000 to 3500 cm^{-1}. This indicates that LPSCl does not undergo a complete hydrolysis reaction when exposed to moisture. Asymmetric stretching (1427 cm^{-1}) and out-of-plane bending (864 cm^{-1}) of the carbonate anion were only observed in the air exposed sample, suggesting the formation of carbonate species due to a reaction with CO_2 when exposed to ambient air.[35] The carbonate signals were not observed in the water exposed sample, since LPSCl was not openly exposed to ambient air for a prolonged period of time in this case. As neither Li_2CO_3 nor $LiHCO_3$ is observed in the XRD pattern, the carbonate species may be amorphous or formed only on the surface and in low amounts.[36, 37] After the heat treatment, strong PO_4^{3-} asymmetric stretching peaks appear near 1030 cm^{-1}, in agreement with the Li_3PO_4 formation observed using XRD.[38] The pristine LPSCl shows strong PS_4^{3-} stretching near 425 cm^{-1} in Raman (**Figure 3b**).[39] After exposure to air, a strong peak at 218 cm^{-1} appears and this implies the formation of oxysulfides. The sample exposed to water shows only a minor peak shift, but the peak shape is significantly narrowed compared to that of pristine LPSCl. This indicates the possible formation of different major oxysulfide species from the air-exposed sample. After the heat treatment for both exposed samples, the PS_4^{3-} signal is partially recovered. Oxysulfides can still be observed, as they all exhibit a shoulder sitting around 220 cm^{-1}. However, as the Raman signals of PS_4^{3-} and oxysulfides are close to each other, other characterization methods are required to reveal the specific details on the structure of exposed LPSCl.

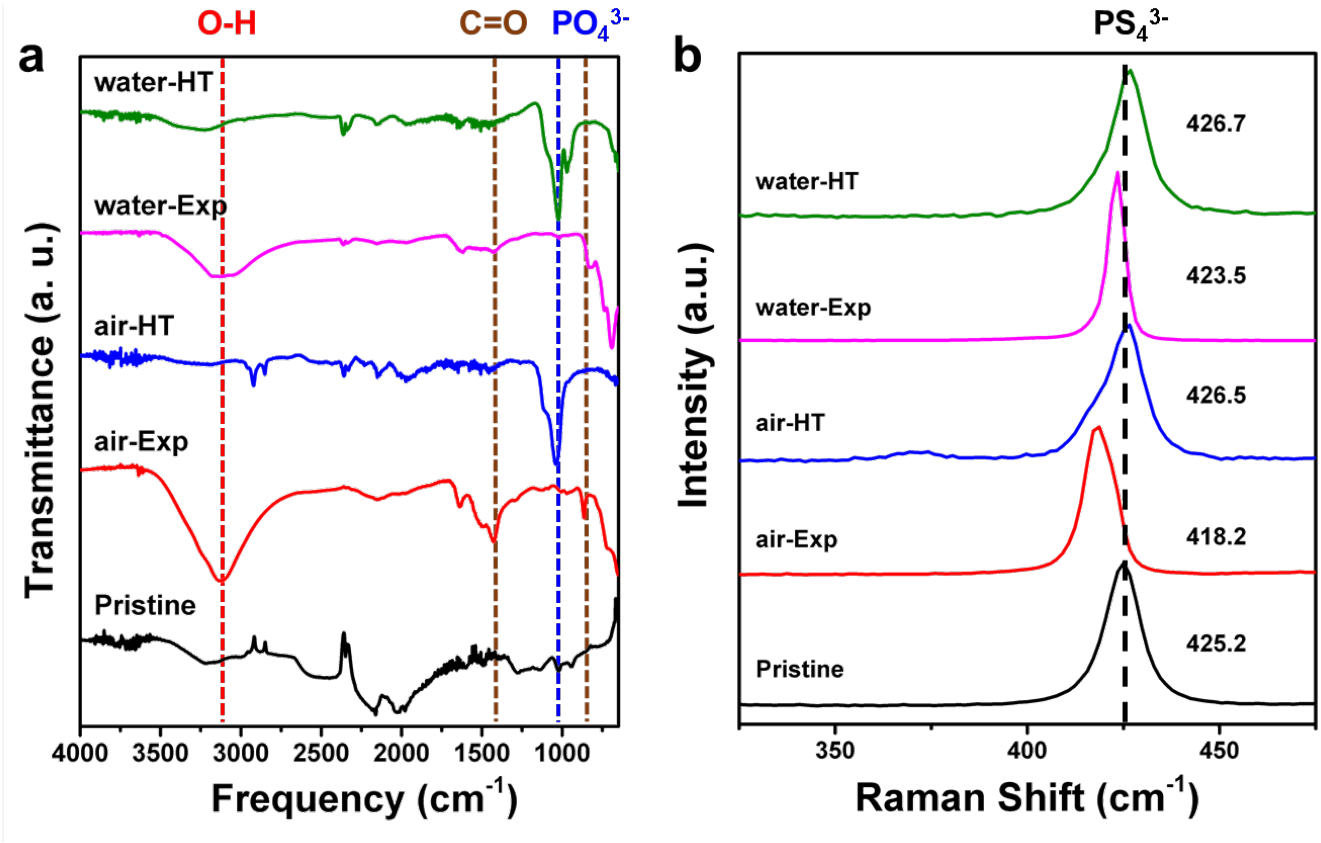

Figure 3. a) FTIR and b) Raman spectra of the pristine, exposed and heat-treated LPSCl samples. The main peaks of interested are represented by dashed lines on the FTIR spectra, while the Raman spectra only shows the PS_4^{3-} peak.

To provide more insights on the hydration structure of exposed LPSCl, ^{31}P NMR was conducted (**Figure 4a**). The pristine LPSCl exhibits broad peaks from ~ 85 - 81 ppm, as previously reported in literature .[40-42] The peaks are assigned to PS_4^{3-} tetrahedra that are broadened by anion disorder from substitutional mixing of Cl and S atoms.[43] After either air or water exposure, the LPSCl peaks largely disappear and are replaced by two sharper peaks at 83.2 and 76.7 ppm, which are assigned to hydrated POS_3^{3-} and hydrated $PO_2S_2^{3-}$ tetrahedra, respectively. The mixed oxysulfide phosphorous tetrahedra ^{31}P chemical shift values agree with previous reports.[44] Both peaks are present in $\{^1H\}$-^{31}P cross polarization measurements, indicating the phosphorous tetrahedra are spatially close to protons and have moderate dipolar coupling (**Figure 4b and 4c**). The air and water exposure appears to create the same hydrated POS_3^{3-} and $PO_2S_2^{3-}$ tetrahedra, evident by the respective peaks having the same chemical shift anisotropy values (**Figure 4b and 4c**) and identical cross-polarization buildup curves (**Figure S7**). After air exposure, close to 60% of the original LPSCl remains while most degradation produces the hydrated POS_3^{3-} tetrahedra and a minor amount of hydrated $PO_2S_2^{3-}$ tetrahedra (**Table S3**). The LPSCl phase may become disordered after air exposure and thus is not observed in the XRD pattern (**Figure S4**). The hydrated and

mixed anion $PO_xS_y^{3-}$ tetrahedra are marked by very long spin-lattice relaxation times (T_1) on the order of 100's of seconds, whereas LPSCl has a T_1 of about ~4 s. This extreme difference of T_1 values can be used as a spectral filter by saturating the signal of the slow relaxing hydrated phases by using a short recycle delay (~15 s) during acquisition. The relaxation filter removes the signal from non-conducting phases and leaves the signal of the fast Li ion conductor LPSCl, demonstrating LPSCl remains after air exposure (**Figure S8**).

Further information about the state of hydration of the hydrated POS_3^{3-} and $PO_2S_2^{3-}$ phases can be obtained by ^1H-^{31}P heteronuclear correlation (HETCOR) measurements (**Figure 4d**). Both phases are spatially close to water molecules (^1H δ ~ 4.9 ppm) and the hydrated POS_3^{3-} tetrahedra are also close to -OH groups (^1H δ ~ 0 ppm). The difference in neighboring water and hydroxyl groups between the phases suggests some degree of microstructural heterogeneity caused by regions of more rapid degradation. Contrast to air exposure where some LPSCl remains, exposure to water eliminates the LPSCl signal from the ^{31}P spectra indicating the LPSCl is completely degraded, in agreement with XRD results and the dramatically lowered ionic conductivity. Water exposure converts most of the sample to the hydrated $PO_2S_2^{3-}$ phase with a minor amount of the hydrated POS_3^{3-} phase. After heat treatment, about 67% of LPSCl is reformed in the air exposed sample while only 47% is recovered for the water exposed (**Table S3**). The result is close to the phase ratios of LPSCl : Li_3PO_4 (^{31}P NMR only detects P containing phases) obtained from XRD results (64% for the air exposed sample and 20% for the water exposed sample). The T_1 values for the reformed LPSCl after heat treatment are comparable to the pristine LPSCl, in agreement with the similar recovery observed for the ionic conductivity. The sulfur loss from exposure to moisture/water produces the oxysulfide phosphorous tetrahedra which then largely disassociate into PO_4^{3-} and PS_4^{3-} tetrahedra after heat treatment with only minute amounts of oxysulfide tetrahedra ($PO_2S_2^{3-}$ and PO_3S^{3-}) remaining (**Table S3**). A significant amount of Li_3PO_4 (δ_{iso} = 9.3 ppm[45, 46]) is formed after heat treatment from both air and water exposed samples, in agreement with XRD and FTIR results. Due to the extreme sulfur loss in the water exposed sample, more sulfur deficient phases are formed (**Figure S9**) like $P_2S_7^{4-}$ (δ_{iso} =91.5 ppm), PSO_3^{3-} (δ_{iso} =35 ppm) and another PO_4^{3-} phase (δ_{iso} =11 ppm).[44, 47] This other PO_4^{3-} phase has a slightly higher chemical shift than Li_3PO_4, suggesting it may have a higher coordination to S atoms within its second nearest neighbor shell. As such this resonance could arise from PO_4^{3-} tetrahedra embedded within sulfur rich regions and further speaks to the microstructural heterogeneity. $\{^1H\}$-^{31}P cross polarization was attempted on the heat-treated samples but did not produce appreciable signal, indicating the samples have been completely dehydrated.

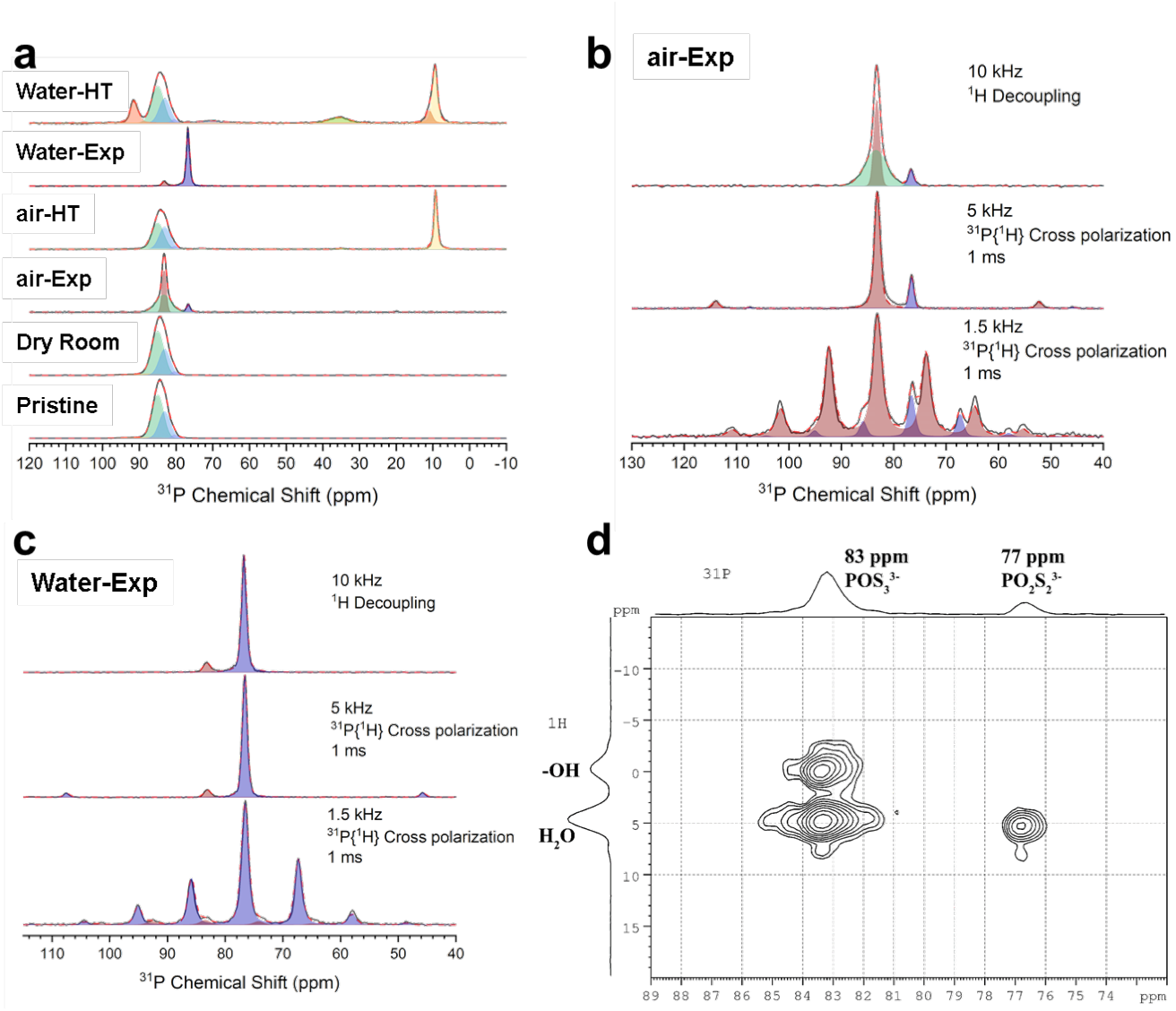

Figure 4. a) ^{31}P MAS NMR spectra of the pristine, dry room, exposed and heat-treated LPSCl samples. Comparison of ^{31}P spectra with ^{1}H decoupling (top) to ^{31}P{^{1}H} cross polarization spectra of b) air-Exp and c) water-Exp samples at spinning speeds of 5 (middle) and 1.5 kHz (bottom). Sideband analysis was conducted at both spinning speeds of the CP measurement to determine the chemical shift anisotropy (CSA) of the two hydrated oxysulfide phases, δ_{iso}=76.8 ppm, $\Delta\delta$ = 30.3 ppm, η = 0.63 (δ_{11}=97 ppm, δ_{22}= 73.0 ppm, δ_{33}= 60.3 ppm) and δ_{iso}=83.5 ppm, $\Delta\delta$ = -34.3 ppm, η = 0.94 (δ_{11}=105.7 ppm, δ_{22}= 84.2 ppm, δ_{33}= 60.6 ppm). The CSA is defined with the Haeberlen convention where the principal components are ordered by $|\delta_{zz} - \delta_{iso}| \geq |\delta_{xx} - \delta_{iso}| \geq |\delta_{yy} - \delta_{iso}|$, and where $\delta_{iso} = \frac{1}{3}(\delta_{xx} + \delta_{yy} + \delta_{zz})$; $\Delta\delta = \delta_{zz} - (\delta_{xx} + \delta_{yy})/2$; $\eta = \frac{\delta_{yy} - \delta_{xx}}{\delta_{zz} - \delta_{iso}}$. The CSA is also provided in the standard convention within parenthesis where the principal components are defined by $\delta_{11} \geq \delta_{22} \geq \delta_{33}$. d) ^{1}H-^{31}P HETCOR NMR contour plot showing ^{1}H-^{31}P correlations through dipolar coupling of the air exposed sample. The HETCOR measurement reveals the oxysulfide phosphorous tetrahedra are spatially close to water

and hydroxyl groups.

^{7}Li NMR was also performed to track the decomposition from the perspective of Li ions. Unfortunately, ^{7}Li spectra are less elucidating chemically relative to ^{31}P NMR because of strong homonuclear dipolar coupling considerably broadens the signal, ^{7}Li has a narrow chemical shift range, and the rapid motion of Li ions over many crystallographically distinct sites in LPSCl causes chemical exchange meaning only the average chemical shift to be resolvable. Despite these limitations, some important insights are still available from ^{7}Li NMR such as being able to track the formation of LiCl. The ^{7}Li spectra (**Figure S10**) of pristine LPSCl is a very narrow peak centered around 1.52 ppm, in agreement with previous reports.[42] Because of the rapid Li ion motion, the Li ion experiences many chemical environments within the NMR experimental timeframe thus only one or two peaks are observable. However, the location of the narrowed peaks still provides insight to the local Li chemical environments. After air exposure the peak shifts to ~1.3 ppm and another peak arises at 1.24 ppm indicating there are two separate regions of rapid Li conduction. After heat treatment of the air exposed sample the narrow peak shifts back to 1.49 ppm, very close to the pristine LPSCl peak. The slightly lower frequency indicates the Li ions are moving through sites with slightly less sulfur. This can also explain the more dramatic lower frequency shift (peak at 1.36 ppm) in the heat-treated water exposed sample that has higher sulfur loss. Beyond the subtle changes in the fast Li ion conducting peaks, the formation of decomposition products like LiCl and Li_2S are more obvious (**Figure S11**). After exposure, a broad peak at −1.1 ppm corresponding to LiCl becomes prominent. As evident from ^{31}P NMR, water exposure eliminates the sharp peak LiPSCl signal leaving the LiCl peak and a very broad peak at 0.68 ppm that is likely immobile Li within the hydrated oxysulfide phosphorous phases. ^{7}Li within phosphorous oxide environments have chemical shifts between 1 to 0.14 ppm, so a slight shielding indicates the presence of more oxygen in the Li coordination sphere.[45, 46] After heat treatment, along with the reformation of LPSCl, the LiCl peak remains along with a prominent shoulder at 2 ppm that is assigned to Li_2S.[48] The signal for Li_3PO_4 is not resolvable but is likely contributing to the additional broadening of the peaks between 1 – 0 ppm. ^{7}Li spin-lattice relaxation times were measured on all the samples and found largely similar results as obtained by ^{31}P SLR measurements (**Table S3**). The ^{7}Li T_1 of LPSCl is on the order of 100-200 ms while oxysulfide and Li_2S phases have T_1 values around 9 s and LiCl has a T_1 of ~26 s.

As both IR and NMR spectroscopy indicate that LPSCl becomes hydrated, it is worth investigating the dehydration process during the heat treatment. Therefore, a combination of TGA, DSC, and MS were conducted to monitor the decomposition processes and gas evolution of H_2O, H_2S, and CO_2 during heating. **Figure S12** presents the TGA / DSC – MS of a pristine LPSCl sample. Little to no mass loss, endothermic, or exothermic reactions were observed in TG and DSC curves, indicating that the material is stable throughout the whole temperature range of the experiment. Nevertheless, the minor gas evolution observed can be explained by the short exposure to air during sample transfer to the instrument. As such, the pristine sample is used as the baseline when comparing the results of the air exposed samples. After the exposure, both the air (**Figure 5a**) and water exposed (**Figure S13**) samples exhibited significant mass loss in the TG curves and each of these mass losses is

accompanied by gas evolution and endothermic or exothermic reactions. On the DSC curve, the reactions for both samples were located near 140, 300, and 430°C, with the main mass loss and gas evolution occurring at around 140°C. Both H_2O and H_2S evolution were observed and thus both dehydration and hydrolysis (reaction between LPSCl and hydrated water at elevated temperature, generating H_2S) reactions take place at this temperature. As the DSC curve indicates an overall endothermic result, the dehydration process is dominating over the hydrolysis (dehydration reactions are endothermic, while hydrolysis reactions are exothermic). The shapes of the curves are different for the air and water exposed samples, consistent with the different major hydrated species detected in the two samples, as shown in the ^{31}P NMR results. At 296°C, both samples exhibit an exothermic peak accompanied with H_2O and H_2S evolution. This indicates that the hydrolysis reaction dominates at this temperature. There is an extra exothermic reaction at 332°C (accompanied with CO_2 evolution) in the air exposed sample, suggesting that a carbonate species decomposes at this temperature. This reaction was not observed in the water exposed sample, as no carbonates formed under these conditions. This is consistent with the FTIR results presented in **Figure 3a**. For both samples, no gas evolution was detected after 350°C, suggesting the complete removal of H_2O and CO_2. One endothermic reaction occurs around 430°C. As there is no mass loss and gas evolution associated with this reaction, this is purely a phase transformation reaction and it requires further characterization.

To confirm the reactions during the heating process, the air exposed sample was heat treated at selected temperatures: 200, 350, and 450°C, chosen according to the TGA / DSC results (**Figure S14a**). FTIR (**Figure 5b**), XRD (**Figure 5c**), and EIS (**Figure S14b-d**) were conducted after heat treatment. When heated to 200 °C, OH stretching and CO_3^{2-} vibrations still appear on the FTIR spectra, but these signals disappear after heating above 350 °C. After heating to 450 °C, the PO_4^{3-} stretching signal was observed, indicating the formation of Li_3PO_4 at this temperature. Moreover, the XRD data also indicates the reformation of LPSCl at this temperature, as the diffraction pattern is similar to that of the air exposed sample heated to 550°C (air-HT). The EIS measurements also show that the ionic conductivity increased by 3 orders of magnitude after the heat treatment at 450°C. Both results imply that the reformation of LPSCl occurs at approximately 430°C.

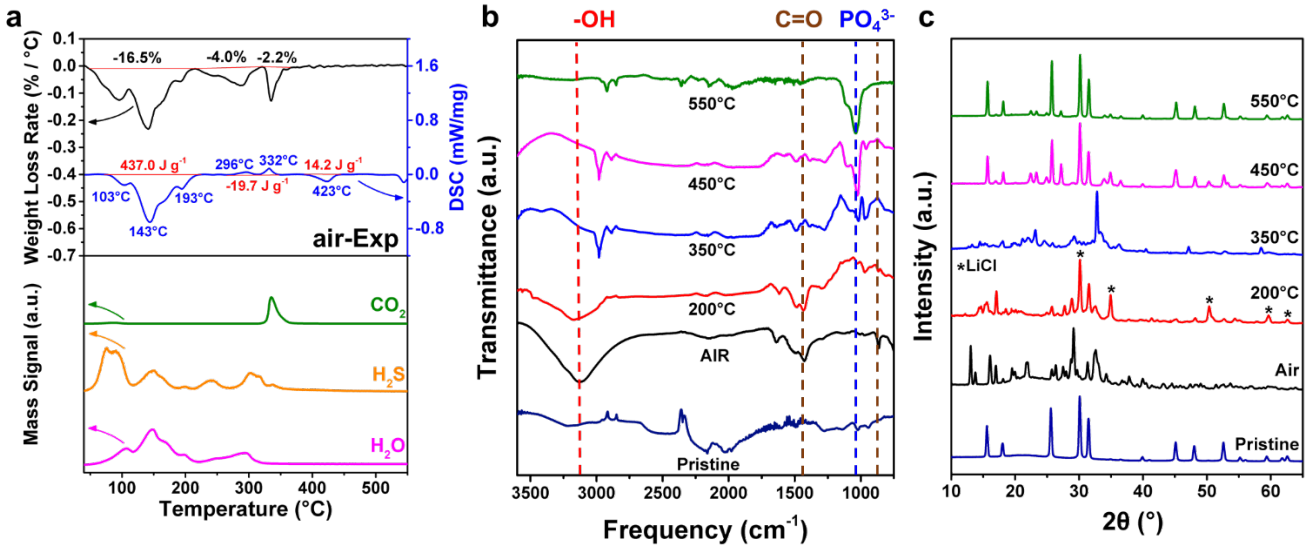

Figure 5. a) Coupled TGA / DSC and mass spectrometry measurements of the air exposed sample (air-Exp). b) FTIR spectra and c) XRD pattern of the air-Exp sample heat treated at different temperatures.

The wide array of characterization results show that LPSCl is most significantly affected by moisture exposure. As such, LPSCl may show improved stability if the humidity of the atmosphere is controlled. To prove this hypothesis, LPSCl was exposed to air in a dry room with a dew point of −45°C for 1, 2, 3, and 24 hours. **Figure 6a** shows the ionic conductivity as a function of the exposure time, the corresponding Nyquist plots are presented in **Figure S15a**. The electrolyte conductivity decreased linearly during the first 3 hours of exposure, but maintained a value of 2.33 x 10^{-3} S cm^{-1} after 24 hours of exposure, which is 3 orders of magnitude higher than air-Exp sample. The ionic conductivity of dry room exposed LPSCl can be partially recovered to 2.77 x 10^{-7} S cm^{-1} after a heat treatment at 550°C for 8 hours. As shown in **Figure S15b**, the electronic conductivity of LPSCl did not increase after dry room exposure.

XRD (**Figure S16**), Raman (**Figure S17**), ^{31}P NMR (**Figure 4a**) and ^{7}Li NMR (**Figure S10**) show no large-scale decomposition happened to the material during exposure in the dry room environment even after 24 hours, as these data are very similar to those of the pristine LPSCl sample. Nevertheless, FTIR (**Figure S18**) shows an increasing CO_3^{2-} signal with increasing exposure time, indicating the formation of carbonate species. Attempts at measuring ^{13}C-^{1}H cross-polarization NMR to further characterize the carbonate species were unsuccessful, thus indicating the quantity of carbonates is extremely low or the carbonates are not spatially close to protons. The CO_2 evolution peak observed near 330°C in the TGA/DSC – MS measurements (**Figure S19**) also confirm the existence of carbonates. Therefore, carbonate formation may explain the ionic conductivity drop. After removing carbonates with a heat treatment at 550°C for 8 hours, as suggested by the TGA results, the CO_3^{2-} signal no longer appears in the FTIR spectrum and the ionic conductivity is also mostly recovered. However, there is evidence of LPSCl decomposition in the FTIR spectrum (PO_4^{3-} signal at 1030 cm^{-1}) and the XRD pattern (LiCl, Li_2S, and Li_3PO_4 peaks are identified), which may explain why the ionic conductivity is not fully recovered.

Lastly, the dry room adaptability of LPSCl was examined by comparing the performance of two $LiNi_{0.8}Co_{0.1}Mn_{0.1}O_2$ (NCM811) | LPSCl | LiIn all-solid-state cells, fabricated with either the pristine or the dry room exposed (24 hours) LPSCl. Both cells exhibit similar 1st cycle charge capacity of around 214 mAh g^{-1} and 1st cycle Coulombic efficiency (CE) of 78.1% (**Figure 6b**). Moreover, the cell performance (**Figure 6c**) in further cycles (CE and capacity retention) are also similar, proving that this particular sulfide SSE is dry room compatible.

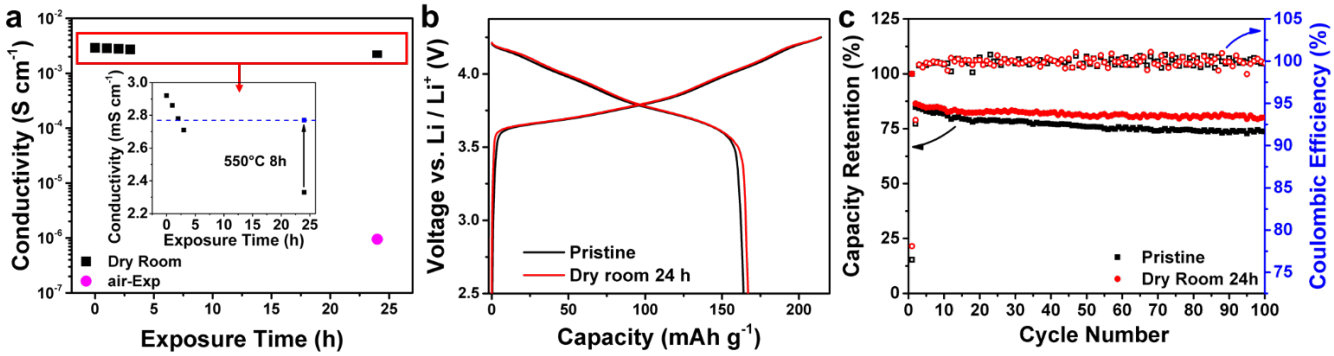

Figure 6. a) Ionic conductivity of pristine LPSCl, LPSCl samples exposed in a dry room for 1, 2, 3, 24 hours, a heat-treated sample following 24 hours of dry room exposure, and air-exposed LPSCl. b) 1st cycle voltage profiles, c) capacity retention and Coulombic efficiency of NCM811 | LPSCl | LiIn cells assembled using pristine or 24h dry room exposed LPSCl electrolytes.

Conclusion

This study elucidates the degradation mechanism of a sulfide electrolyte, LPSCl, during exposure to air and moisture. The effects of post-heat treatment at 550°C on the exposed LPSCl were also studied. As evidenced by our results, both hydration and hydrolysis reactions occur during the exposure. To investigate the mechanism in detail, XRD, XPS, Raman, FTIR, and NMR characterizations were conducted at various exposure and heat treatment states. When exposed to ambient air and water, LPSCl not only partially hydrolyzes to generate H_2S, resulting in permanent sulfur loss, but also forms two different hydrated species and carbonates (depending on the amount of water). Heat-treatment at 350°C can fully dehydrate LPSCl and completely decompose the carbonates. Nevertheless, the hydrolysis reaction can still occur during the heat treatment. LPSCl can be partially recovered when heated to 450°C, during which LiCl, Li_2S and Li_3PO_4 are also formed, accompanying the sulfur loss due to the hydrolysis reaction. When exposed to a dry room atmosphere, where the level of moisture is strictly controlled (around 100 ppm), LPSCl does not undergo significant decomposition and retains most of its ionic conductivity even after 24 hours of exposure. Nevertheless, minor carbonate formation still occurs, explaining the slight reduction in conductivity. These carbonate species can also be removed via heat treatment at 550°C. Finally, the dry room exposed LPSCl was used to fabricate a NCM811 | LPSCl | LiIn all solid-state cell and compared with the pristine electrolyte. Both cells showed similar electrochemical performance and capacity retention, indicating that this argyrodite electrolyte is dry room compatible. Our work thus provides a foundation for the academic field to move forward and focus on developing scalable ASSBs.

Conflict of interest

There are no conflicts to declare.

Acknowledgement

This work was partially supported by LG Chem through the Battery Innovation Contest (BIC) program as well as the Energy & Biosciences Institute through the EBI-Shell program. Z.C. acknowledges funding from the start-up fund support from the Jacob School of Engineering at University of California San Diego. Y.S.M. acknowledges funding support from Zable Endowed Chair Fund. Part of this work was performed at the San Diego Nanotechnology Infrastructure (SDNI) of the UCSD, a member of the National Nanotechnology Coordinated Infrastructure, supported by the National Science Foundation (Grant ECCS-1542148). Part of this work was performed under the auspices of the U.S. Department of Energy by Lawrence Livermore National Laboratory under contract DE-AC52-07NA27344, LLNL-JRNL-827313. The authors acknowledge the use of facilities and instrumentation supported by NSF through the UC San Diego Materials Research Science and Engineering Center (UCSD MRSEC), grant # DMR-2011924, and the use of facilities and instrumentation at the UC Irvine Materials Research Institute (IMRI) supported in part by the National Science Foundation Materials Research Science and Engineering Center program through the UC Irvine Center for Complex and Active Materials (DMR-2011967).

References

1. T. Chen, Y. Jin, H. Lv, A. Yang, M. Liu, B. Chen, Y. Xie and Q. Chen, *Trans. Tianjin Univ.*, 2020, **26**, 208-217.
2. Y. Horowitz, C. Schmidt, D.-h. Yoon, L. M. Riegger, L. Katzenmeier, G. M. Bosch, M. Noked, Y. Ein-Eli, J. Janek and W. G. Zeier, *Energy Technology*, 2020, **8**, 2000580.
3. Y. S. Jung, D. Y. Oh, Y. J. Nam and K. H. Park, *Isr. J. Chem.*, 2015, **55**, 472-485.
4. K. Kerman, A. Luntz, V. Viswanathan, Y.-M. Chiang and Z. Chen, *J. Electrochem. Soc.*, 2017, **164**, A1731.
5. H. Lee, P. Oh, J. Kim, H. Cha, S. Chae, S. Lee and J. Cho, *Adv. Mater.*, 2019, **31**, 1900376.
6. K. J. Kim, M. Balaish, M. Wadaguchi, L. Kong and J. L. Rupp, *Adv. Energy Mater.*, 2021, **11**, 2002689.
7. Y. Seino, T. Ota, K. Takada, A. Hayashi and M. Tatsumisago, *Energy Environ. Sci.*, 2014, **7**, 627-631.
8. N. Kamaya, K. Homma, Y. Yamakawa, M. Hirayama, R. Kanno, M. Yonemura, T. Kamiyama, Y. Kato, S. Hama and K. Kawamoto, *Nat. Mater.*, 2011, **10**, 682.
9. J. Janek and W. G. Zeier, *Nat. Energy*, 2016, **1**, 1-4.
10. K. Takada, M. Osada, N. Ohta, T. Inada, A. Kajiyama, H. Sasaki, S. Kondo, M. Watanabe and T. Sasaki, *Solid State Ionics*, 2005, **176**, 2355-2359.
11. W. D. Jung, M. Jeon, S. S. Shin, J.-S. Kim, H.-G. Jung, B.-K. Kim, J.-H. Lee, Y.-C. Chung and H. Kim, *ACS omega*, 2020, **5**, 26015-26022.
12. T. Ohtomo, A. Hayashi, M. Tatsumisago and K. Kawamoto, *J. Non-Cryst. Solids*, 2013, **364**, 57-61.
13. T. Kimura, A. Kato, C. Hotehama, A. Sakuda, A. Hayashi and M. Tatsumisago, *Solid State Ionics*, 2019, **333**, 45-49.
14. Z. Zhang, J. Zhang, Y. Sun, H. Jia, L. Peng, Y. Zhang and J. Xie, *Journal of Energy Chemistry*, 2020, **41**, 171-176.
15. X. Li, J. Liang, K. R. Adair, J. Li, W. Li, F. Zhao, Y. Hu, T.-K. Sham, L. Zhang and S. Zhao, *Nano Lett.*, 2020, **20**, 4384-4392.
16. S. Ahmed, P. A. Nelson and D. W. Dees, *J. Power Sources*, 2016, **326**, 490-497.
17. D. Li, L. Cao, C. Liu, G. Cao, J. Hu, J. Chen and G. Shao, *Appl. Surf. Sci.*, 2019, **493**, 1326-1333.
18. C. Yu, S. Ganapathy, J. Hageman, L. van Eijck, E. R. van Eck, L. Zhang, T. Schwietert, S. Basak, E. M. Kelder and M. Wagemaker, *ACS applied materials & interfaces*, 2018, **10**, 33296-33306.
19. C. Yu, L. van Eijck, S. Ganapathy and M. Wagemaker, *Electrochim. Acta*, 2016, **215**, 93-99.
20. S. Wang, Y. Zhang, X. Zhang, T. Liu, Y.-H. Lin, Y. Shen, L. Li and C.-W. Nan, *ACS applied materials & interfaces*, 2018, **10**, 42279-42285.
21. X. Randrema, C. Barcha, M. Chakir, V. Viallet and M. Morcrette, *Solid State Sciences*, 2021,

106681.
22. W. Arnold, D. A. Buchberger, Y. Li, M. Sunkara, T. Druffel and H. Wang, *J. Power Sources*, 2020, **464**, 228158.
23. J. Auvergniot, A. Cassel, D. Foix, V. Viallet, V. Seznec and R. Dedryvère, *Solid State Ionics*, 2017, **300**, 78-85.
24. A.-K. Hatz, R. Calaminus, J. Feijoo, F. Treber, J. Blahusch, T. Lenz, M. Reichel, K. Karaghiosoff, N. M. Vargas-Barbosa and B. V. Lotsch, *ACS Appl. Energy Mater.*, 2021, **4**, 9932-9943.
25. F. Friedrich, B. Strehle, A. T. Freiberg, K. Kleiner, S. J. Day, C. Erk, M. Piana and H. A. Gasteiger, *J. Electrochem. Soc.*, 2019, **166**, A3760.
26. J. P. Yesinowski and H. Eckert, *J. Am. Chem. Soc.*, 1987, **109**, 6274-6282.
27. D. Massiot, F. Fayon, M. Capron, I. King, S. Le Calvé, B. Alonso, J. O. Durand, B. Bujoli, Z. Gan and G. Hoatson, *Magn. Reson. Chem.*, 2002, **40**, 70-76.
28. M. A. Kraft, S. P. Culver, M. Calderon, F. Böcher, T. Krauskopf, A. Senyshyn, C. Dietrich, A. Zevalkink, J. r. Janek and W. G. Zeier, *J. Am. Chem. Soc.*, 2017, **139**, 10909-10918.
29. A. Ievină, M. Straumanis and K. Karlsons, *Z. Phys. Chem.*, 1938, **40**, 146-150.
30. W. Buehrer, F. Altorfer, J. Mesot, H. Bill, P. Carron and H. Smith, *J. Phys.: Condens. Matter*, 1991, **3**, 1055.
31. N. I. Ayu, E. Kartini, L. D. Prayogi and M. Faisal, *Ionics*, 2016, **22**, 1051-1057.
32. H. Peisert, T. Chassé, P. Streubel, A. Meisel and R. Szargan, *J. Electron. Spectrosc. Relat. Phenom.*, 1994, **68**, 321-328.
33. A. Vizintin, M. Lozinšek, R. K. Chellappan, D. Foix, A. Krajnc, G. Mali, G. Drazic, B. Genorio, R. m. Dedryvère and R. Dominko, *Chem. Mater.*, 2015, **27**, 7070-7081.
34. Z. Tai, W. Zhu, M. Shi, Y. Xin, S. Guo, Y. Wu, Y. Chen and Y. Liu, *J. Colloid Interface Sci.*, 2020, **576**, 468-475.
35. S. Yin, Y. Zeng, C. Li, X. Chen and Z. Ye, *ACS applied materials & interfaces*, 2013, **5**, 12876-12886.
36. H. Chung, Z. Lebens-Higgins, B. Sayahpour, C. Mejia, A. Grenier, G. E. Kamm, Y. Li, R. Huang, L. F. Piper and K. W. Chapman, *J. Mater. Chem. A*, 2021, **9**, 1720-1732.
37. N. V. Faenza, L. Bruce, Z. W. Lebens-Higgins, I. Plitz, N. Pereira, L. F. Piper and G. G. Amatucci, *J. Electrochem. Soc.*, 2017, **164**, A3727.
38. S. M. Benoy, S. Singh, M. Pandey and B. Manoj, *Materials Research Express*, 2020, **6**, 125624.
39. D. H. Tan, A. Banerjee, Z. Deng, E. A. Wu, H. Nguyen, J.-M. Doux, X. Wang, J.-h. Cheng, S. P. Ong and Y. S. Meng, *ACS Appl. Energy Mater.*, 2019, **2**, 6542-6550.
40. I. Hanghofer, B. Gadermaier and H. M. R. Wilkening, *Chem. Mater.*, 2019, **31**, 4591-4597.
41. H. J. Deiseroth, S. T. Kong, H. Eckert, J. Vannahme, C. Reiner, T. Zaiß and M. Schlosser, *Angew. Chem.*, 2008, **120**, 767-770.

42. D. H. Tan, E. A. Wu, H. Nguyen, Z. Chen, M. A. Marple, J.-M. Doux, X. Wang, H. Yang, A. Banerjee and Y. S. Meng, *ACS Energy Letters*, 2019, **4**, 2418-2427.
43. I. Hanghofer, M. Brinek, S. Eisbacher, B. Bitschnau, M. Volck, V. Hennige, I. Hanzu, D. Rettenwander and H. Wilkening, *PCCP*, 2019, **21**, 8489-8507.
44. A. Hayashi, H. Muramatsu, T. Ohtomo, S. Hama and M. Tatsumisago, *J. Alloys Compd.*, 2014, **591**, 247-250.
45. G. O. Hartley, L. Jin, B. J. Bergner, D. S. Jolly, G. J. Rees, S. Zekoll, Z. Ning, A. T. Pateman, C. Holc and P. Adamson, *Chem. Mater.*, 2019, **31**, 9993-10001.
46. M. A. Marple, T. A. Wynn, D. Cheng, R. Shimizu, H. E. Mason and Y. S. Meng, *Angew. Chem. Int. Ed.*, 2020, **59**, 22185-22193.
47. M. Murakami, K. Shimoda, S. Shiotani, A. Mitsui, K. Ohara, Y. Onodera, H. Arai, Y. Uchimoto and Z. Ogumi, *The Journal of Physical Chemistry C*, 2015, **119**, 24248-24254.
48. M. U. Patel, I. Arcon, G. Aquilanti, L. Stievano, G. Mali and R. Dominko, *ChemPhysChem*, 2014, **15**, 894-904.